Carbon 196 (2022) 1035–1046

Contents lists available at ScienceDirect

Carbon

journal homepage: www.elsevier.com/locate/carbon

Formamidinium halide salts as precursors of carbon nitrides

Isabel Ciria-Ramos [a], Nuria Navascués [a], Fatou Diaw [a], Clarisse Furgeaud [a,b], Raul Arenal [a,b,c], Alejandro Ansón-Casaos [d], Marta Haro [a,*], Emilio J. Juarez-Perez [a,c,**]

[a] Instituto de Nanociencia y Materiales de Aragón (INMA), CSIC-Universidad de Zaragoza, Zaragoza, 50009, Spain
[b] Laboratorio de Microscopias Avanzadas (LMA), U. Zaragoza, C/ Mariano Esquillor S/n, 50018, Zaragoza, Spain
[c] Aragonese Foundation for Research and Development (ARAID). Government of Aragon, Zaragoza, 50018, Spain
[d] Instituto de Carboquímica, CSIC, Zaragoza, 50018, Spain

ARTICLE INFO

Keywords:
Carbon nitride
Pyrolysis
Formamidinium cation
Perovskite solar cells

ABSTRACT

Pyrolysis of formamidinium halide salts (FAI, FABr) results in a new type of amorphous carbon nitride materials with a mass fraction of 40–50% nitrogen content. Pyrolysis temperature drives final chemical composition, morphology, optical and electrical properties of the material independently of the halide precursor and identifying triazine ring, instead of typical heptazine unit, as the main building block of this material. We elaborated a temperature dependent mechanism of formation for these materials and foresee its potential value as native passivation layer in the field of perovskite solar cells.

1. Introduction

Carbon nitrides (CNs) are a family of compounds composed by carbon, nitrogen and hydrogen atoms arranged as triazine or heptazine rings units linked through tri-coordinated N atoms and disposed to form structures ranging from condensed crystalline (graphitic) phases to disordered polymeric phases [1]. Different approaches are available to synthesize CNs including physical/chemical vapor deposition and pyrolysis/condensation of carbon and nitrogen containing precursors as cyanamide, cyanide salts, urea, guanidinium salts, s-triazines, s-heptazines and thiocyanates [1–3]. Precursor type and synthetic procedure tune the electronic properties of CN. Conventional yellow/orange CN presents a band gap energy range between 2.5 and 2.8 eV, but as condensation increases, crosslinking increases and terminal amine groups are lost, which leads to band gap narrowing and the formation of more disordered structures. This causes a dark brown or even black color like graphite analogs [4,5]. Considering the possibilities of modifying the electronic, optical and chemical properties, a large number of commercially available precursors and a remarkable chemical resistance, CN materials have a relevant place at the forefront of research for their potential application in the area of free-metal catalysis, diamond-like electro-thermal materials and energy storage/conversion [6]. Furthermore, unlike other inorganic elements of wide use in the electronic/semiconductor field, CNs are sustainable materials composed of abundant elements in the Earth crust. On the downside, their physical-chemical characterization is difficult and intensive research is needed to establish a precise control of their structure-properties relationships.

In this work, the precursor used for synthesizing CNs is the formamidinium cation (FA^+, $CN_2H_5^+$). According to our bibliographic research, FA^+ has never been used before as a precursor to obtain carbon nitride materials. Then, the pyrolysis of formamidinium halide salts (FAI, FABr) at two different temperatures (630 and 830 °C) under inert atmosphere resulted in amorphous carbon nitride materials with a mass fraction of nitrogen ranging on 40–50%. We characterized the chars by elemental analysis, adsorption isotherms, X-ray diffraction (XRD), infrared spectroscopy (FTIR), Raman spectroscopy, ultraviolet–visible-near IR reflectance spectroscopy (UV–vis-IR), X-ray photoelectron spectroscopy (XPS), ultraviolet photoelectron spectroscopy (UPS), scanning electron microscopy (SEM), energy dispersive X-Ray spectroscopy (EDS), transmission electron microscopy (TEM), electron energy loss spectroscopy (EELS), nuclear magnetic resonance (NMR) and pressure dependent electronic conductivity properties. We elaborated a temperature dependent mechanism of formation to uncover unique properties for these materials different to the conventional "melamine" route to obtain g-C_3N_4 type carbon nitrides.

In recent years, we have attended the astonishing development of emerging perovskite halide-based photovoltaics [7]. Despite excellent

* Corresponding author.
** Corresponding author. Instituto de Nanociencia y Materiales de Aragón (INMA), CSIC-Universidad de Zaragoza, Zaragoza 50009, Spain.
E-mail addresses: mharo@unizar.es (M. Haro), ejjuarezperez@unizar.es (E.J. Juarez-Perez).

https://doi.org/10.1016/j.carbon.2022.05.051
Received 13 April 2022; Received in revised form 17 May 2022; Accepted 24 May 2022
Available online 2 June 2022

recorded efficiencies and low manufacturing energy costs compared to silicon-based PV, the current average lifetime of these devices precludes the ultimate commercial success of this technology [8,9]. Then, we foresee the potential value of this finding to produce a native CN passivation layer on formamidinium-based thin-films for perovskite solar cells close equivalent to the role played by SiO_2 on Si-based solar cells.

2. Materials and methods

2.1. Synthesis of the CN chars

CAUTION! Heat treatment of the FA^+ based starting materials evolve NH_3, cyanogen and other harmful gases [10]. Pyrolysis experiments must be carried out with proper vent which permits these gases to escape safely.

A horizontal tube Carbolite furnace equipped with an inner quartz pipe pyrolyzed 1 g of FAX (X = Br or I) under anoxic and anhydrous conditions flowing a dinitrogen current of 70 cm^3/min. The heating program steps were 1) 1.75 h at room temperature to purge air out, 2) a temperature ramp of 20 °C/min until reach final temperature: 630 °C (low temperature) or 830 °C (high temperature), 3) 1 min of dwelling time at selected final temperature and 4) natural cooling of the sample from the maximum temperature of the experiment to ambient temperature. Then, the black powders with metallic shining obtained after pyrolysis were washed and filtered in a frit number 4 Buchner funnel with 20 mL of deionized water, 20 mL of acetone and 20 mL of ethanol. Then, a vacuum oven dried the samples at 110 °C and 26 mbar during 4 h. The mass yield of the reaction considering only initial C, N and H atom contents from precursor was ~50% and ~20% for low and high pyrolysis temperature, respectively. Names for the four samples are Br630, I630, Br830 and I830 depending on halogenated precursor (FABr or FAI) and highest pyrolysis temperature reached 630 °C (low temperature) or 830 °C(high temperature). The choice of these two pyrolysis temperatures is made on the basis of the thermogravimetry-mass spectrometry measurements for FABr and FAI reported elsewhere [10]. The carbon nitride residue appears probably above 400 °C but only gas release stops above ~550 °C. Then, these two high pyrolysis temperatures (630 and 830 °C) were selected to obtain a carbon nitride highly stable, inert, and degassed material for further characterization.

2.2. Bulk elemental analysis

A Perkin-Elmer EA-2400 Series II microanalyzer determined the bulk chemical composition for C, H and N of the samples stored at ambient conditions.

2.3. Dinitrogen adsorption isotherms

Dinitrogen adsorption isotherms at 77 K in a Micromeritics TriStar 3000 established the specific surface area and pore volume distribution for samples previously out-gassed during 10 h at 200 °C and 20 Pa.

2.4. X-ray diffraction

An Empyrean diffractometer from Panalytical performed powder XRD on samples using Cu Kα radiation (λ = 1.5406 Å) and a PIXcel-1D-Medipix3 detector recording between 10 and 50° 2θ at a scan rate of 0.74°/min and 0.026° scan step. The sample holder was a silicon plate free of diffraction peak or shoulder rotating at 0.5 cycles per second to ensure uniformity in the detected signal. Scherrer equation determined crystallite size of samples using 0.9 as shape factor (spherical particle model). A FWHM of 0.170° for the 30.46° 2θ peak of the standard powder LaB_6 defined the instrumental peak broadening.

2.5. FTIR spectroscopy

A Bruker FTIR Vertex 70 equipped with a diamond ATR top-plate and referenced to the empty sample holder acquired Fourier-transform infrared spectroscopy (FTIR) spectra on samples over an average of 40 scans with a resolution of 4 cm^{-1}. Multipeak fitting for peak deconvolution procedure needed a rubber band type baseline correction using OPUS 5 software from Bruker.

2.6. Raman spectroscopy

An alpha300R WITEC Raman confocal microscope acquired Raman spectra of samples at room temperature exciting at 488 nm and 785 nm laser wavelength at low power (1 mW) to avoid the burn out of the samples (as observed for > 20 mW power excitation).

2.7. UV–vis spectroscopy

A UV-VIS-NIR Jasco V6700 equipped with an ISN-723 integrating sphere and PbS photoconductive cell detector measured total reflectance in the 200–2500 nm range for a ~15% mass fraction sample and reflectance reference powder $BaSO_4$. The Kubelka-Munk transformation of the reflectance data determined the pseudo-absorbance of the samples. The extrapolation to zero y-axis of the Tauc plot (indirect allowed band gap setting) allows an optical bandgap estimation of the samples.

2.8. XPS/UPS

A XPS X-Ray Photoelectron Spectroscopy AXIS SupraTM from Kratos with monochromated Al Kα = 1486.6 eV and UPS He−Iα = 21.22 eV radiation source analyzed electronic transitions on the surface of the samples. A copper tape supported the powered sample before compressed air stream removed the excess of material. The vacuum chamber hosted the sample at pressure below $7{\cdot}10^{-9}$ Torr. A unique O 1s peak ascribed to atmospheric contamination at 531.75 eV [11–13] was the reference peak instead of adventitious carbon peak. The Fermi edge (EF = 0 eV) and Au 4f7/2 (84.0 eV) on a clean Au surface calibrated the binding energy for UPS measurements. The software CasaXPS fitted the peak traces.

2.9. SEM/EDS

A FEG INSPECT 50 from FEI equipped with EDS spectrometer analyzed the non-metallized surface of the samples including elemental analysis.

2.10. STEM/EELS

Transmission electron microscopy (TEM) studies were performed in a FEI Titan Cubed 60–300 kV microscope, working at 80 kV and equipped with a spherical aberration corrector (CETCOR Cs-objective CEOS Company) and a Gatan GIF Tridiem 865 EELS spectrometer. Complementary EDS studies were carried out in a FEI Titan Low_Base 60–300 kV probe corrected TEM, also working at 80 kV and fitted with an Oxford Instruments Ultim Max TLE 100 EDS detector. For the TEM studies, the CN samples were dispersed onto copper grids coated with a holey carbon film. The mass density of the sample has been extracted after EELS data analysis [14–19].

2.11. NMR

A Bruker Avance III 400 MHz Wide Bore spectrometer equipped with a 4 mm CP MAS ^{1}H-BB probe acquired NMR spectra of ~100 mg of samples packed inside a zirconium rotor sealed with a Kel-F cap. The ^{13}C CP spectra were acquired with a MAS rate of 10 kHz, a ramp-CP contact time of 3 ms and 7 s recycle delay.

2.12. Conductivity measurements

A homemade holder consisting of thick isolating Teflon die vertically fixed in a heavy stainless steel support with two Cu pistons measured the electrical conductivity (σ) of powdered samples at room temperature (Fig. S1). A hydraulic press (RIKEN SEIKI P-163) controlled the load applied on the piston (0, 57.0, 115.4 and 173.2 MPa). An Autolab M204 applied four DC voltages (0, 1, 2 and 3 V) measuring the dielectric response over the frequency range of 10^2–10^6 Hz [20]. A fitting of the impedance spectra data on Randles model equivalent circuit determined the resistance of samples (Fig. S2).

3. Results

3.1. Chemical composition analysis

We determined the chemical composition of the samples by 1) elemental bulk analysis and three surface methods, namely 2) XPS survey spectra, 3) EDS-SEM and 4) EDS-TEM (Table 1).

Samples analyzed by bulk chemical analysis left no ashes or uncombusted residues. According to EDS analysis (from SEM and TEM), there were no remnant halide from precursors in the pyrolyzed samples with exception of I630 which showed a contamination trace quantity of iodide (0.04 at %) in XPS survey (Figs. S3 and S4). XPS survey scans found oxygen on samples (2–3 at %). Instead, EDS (SEM and TEM) determined oxygen at trace level. Ambient oxygen after sample preparation caused this natural surface oxidation [11]. Then, the main observation from bulk analysis is that regardless of the halide precursor and pyrolysis temperature, these materials contain a molar ratio of ~55–60% for C, 45-40% of N and 1–2% of H content. The pyrolysis temperature has larger influence than halide type of precursor in the final chemical composition of the chars. Indeed, increasing pyrolysis temperature produced a significant decrease in nitrogen and hydrogen contents. The simultaneous decrease of N and H contents with increasing pyrolysis temperature explains the presence of H in amine and/or imine groups (section 3.4 FTIR) released as NH_3 (g) and HCN(g) at high temperature [10]. The molecular chemical formula for chars at low and high pyrolysis temperature are $CN_{0.85}H_{0.04}$ and $CN_{0.65}H_{0.02}$, respectively. There is an excellent match between bulk chemical analysis and EDS (TEM). Instead, XPS and EDS (SEM) follow the general trend on regards C:N ratio on temperature dependency but overestimating C content because they are inherently techniques characterizing the surface of the sample and few nanometers deep in the material. EELS spectra showed C–K and N–K edges (Fig. S6) and the estimation of the mass density was 2.25, 2.09, 2.16 and 2.17 g/cm^3 for samples Br630, I630, Br830 and I830, respectively. According to chemical composition and density, these chars are not the conventional carbon (IV) nitride C_3N_4 neither N doped carbon materials [3] but tunable composition carbon nitrides $C_xN_yH_z$ [21].

3.2. Textural properties

Adsorption N_2 isotherms of the four samples showed type II isotherms, Fig. 1.

All samples are non-porous with low adsorption capacity just occurring in their surface. BET surface area and total pore volume values (Table 2) as well as t-plot method confirm the lack of relevant micro-,

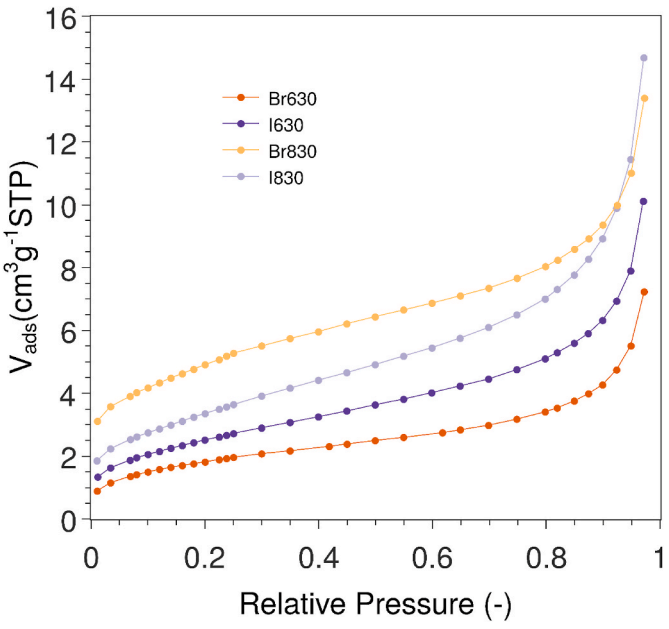

Fig. 1. N_2 adsorption isotherms of Br630, I630, Br830 and I830 samples.

Table 1
Chemical composition reported as atomic fraction (at %) of the samples analyzed by four methods and theoretical composition of formamidinium cation precursor (FA^+, $CH(NH_2)_2^+$).

Analysis type	Sample	C (at %)	H (at %)	N (at %)	O (at %)	Br (at %)	I (at %)	C:N
Bulk Analysis	Br630	51.0 ± 0.4	2.2 ± 0.2	46.8 ± 0.6	–	–	–	1.09
	I630	54.5 ± 1.0	2.0 ± 0.1	43.5 ± 0.9	–	–	–	1.26
	Br830	60.6 ± 0.1	1.4 ± 0.1	38.0 ± 0.1	–	–	–	1.60
	I830	61.2 ± 0.3	1.3 ± 0.1	37.5 ± 0.3	–	–	–	1.63
XPS (survey)	Br630	65.0	–	32.9	2.1	0	0	1.98
	I630	65.5	–	32.3	2.1	0	0.04	2.03
	Br830	69.7	–	27.6	2.8	0	0	2.53
	I830	71.1	–	26.6	2.4	0	0	2.67
EDS (SEM)	Br630	53 ± 1	–	47 ± 1	*	0	0	1.12
	I630	56 ± 1	–	44 ± 1	*	0	0	1.28
	Br830	67 ± 3	–	33 ± 2	*	0	0	2.04
	I830	74 ± 2	–	26 ± 2	*	0	0	2.82
EDS (TEM)	Br630	53.2	–	46.8	*	0	0	1.14
	I630	55.1	–	44.9	*	0	0	1.23
	Br830	60.1	–	39.9	*	0	0	1.51
	I830	61.7	–	38.3	*	0	0	1.61
Theoretical	FA^+	12.5	62.5	25.0	0	0	0	0.5

(–): undetermined. (*): trace.

Table 2
Surface area and total pore volume of the samples.

Sample	Br630	I630	Br830	I830
BET Surface area (m^2/g)	7	9	18	13
Total pore volume (cm^3/g)	0.011	0.016	0.021	0.023

mesoporosity in these materials and their significantly low surface area.

These textural properties are not conclusive on regards of dependence with halogen type employed as precursor but there is a significant increase of BET surface and pore volume for Br830 and I830. This result agrees with a larger quantity of NH_3/HCN released gases [10] activating the material during pyrolysis at higher temperature.

3.3. X-ray diffraction

Powder XRD diffractogram of the four samples showed an amorphous material with a shoulder centered on ~27° 2θ (Fig. 2). Table 3 summarizes the parameters obtained from peak fitting.

Qualitatively, there is no relevant difference between sample diffraction patterns, peak position and type of crystalline domain. The broad reflection, corresponding to d-spacing of ~3.24 Å, is reminiscent of the d_{002} plane found in amorphous carbons or turbostratic carbons [21,22]. Graphitic layers and discotic arrangements with regular ring stacking show this pattern in carbon nitrides [2,3]. The broadness and absence of peaks at lower 2θ indicate amorphous, disordered in-plane and out-plane samples in contrast of the well-defined and sharp d_{002} peak found in poly(triazine imide), poly(heptazine imide), triazine-based graphitic and melon type carbon nitrides [23,24]. Furthermore, small-angle X-ray diffraction (SAXS) pattern confirmed neither diffraction peaks at low angle nor pore structure in these materials [25]. Therefore, XRD data indicates a nanoscopic range order by stacking of fundamental structural units as heptazine motif, sym-triazine ring type or both. Despite FABr and FAI contain Br and I halides, and formamidinium is able to form sym-triazine rings, there is no evidence in the XRD pattern and chemical analysis for the presence of polytriazine imide (PTI) carbon nitrides which intercalates halide ion phases obtained using eutectic molten salt media [26]. Halide precursor has no influence in the pyrolyzed product type obtained. However, quantitative curve fitting showed the width of the peak was broader for the high pyrolysis temperature samples Br830 and I830. It indicates further reduction in the nanoscopic crystallite size in both high temperature

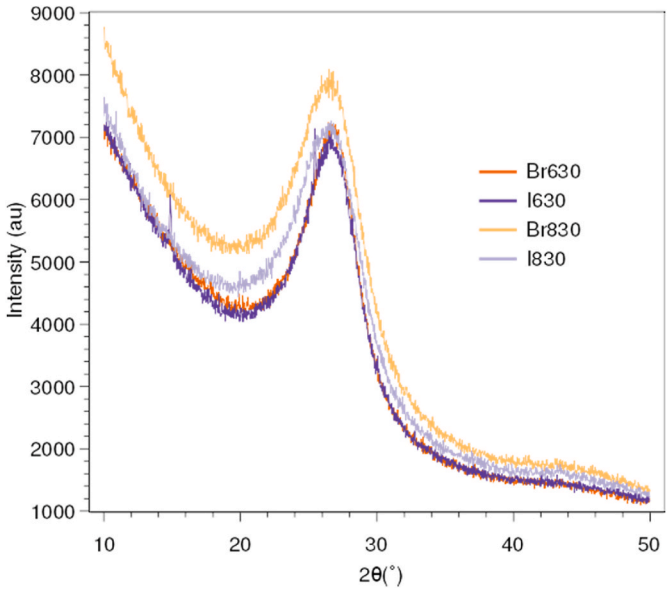

Fig. 2. Powder XRD diffractograms of the four samples.

Table 3
Fittings parameters for the XRD peak.[a].

Sample	Peak maximum (°)	Peak area (au)[b]	FWHM (°)	Scherrer crystallite size (Å)
Br630	27.04	100	4.54	19
I630	26.86	112	5.07	17
Br830	26.82	115	5.54	15
I830	26.80	109	5.53	15

[a]: Curve fittings deposited in the SI file, Fig. S7.[b]: Br630 sample peak area normalized to 100 units.

samples (Br830 and I830) compared to low temperature samples (Br630 and I630) according to the Scherrer equation (Table 3).

3.4. FTIR spectroscopy

FTIR spectra for the high temperature samples Br830 and I830 indicates no significant N–H stretching band in the 3200 cm^{-1} zone (Fig. 3, Table 4). In contrast, low pyrolysis temperature samples show a faded shoulder for this region agreeing with their higher H content detected by bulk elemental analysis and discarding –OH contamination after atmospheric exposure [22,27].

There is neither stretching absorption bands for C_{sp3}-H, C_{sp2}-H nor C_{sp}-H in the 3100–2900 cm^{-1} range indicating that the formamidinium C(H)-$(NH_2)_2$ building block precursor was fully condensed in the material framework. The four samples contain terminal C_{sp}-N_{sp} group (nitrile) at 2220 cm^{-1} [27] and probably oxygen contamination as isocyanate N=C=O at 2167 cm^{-1} [28] but non-terminal groups involving carbodiimides appearing below 2100 cm^{-1} [29]. Also, there is no characteristic sharp absorption at ~800 cm^{-1} corresponding to the heptazine motif [3] but small broad absorption for triazine unit. [13,30].

The large discrepancy between low and high temperature sample appears in the zone denominated the skeletal C_{sp2} – C_{sp2} and C_{sp2} – N_{sp2} mixed modes region. It consists of four main bands at 1584, 1516, 1373, 1250 cm^{-1} for Br630 and I630 collapsing in two broader bands at 1516 and 1195 cm^{-1} for Br830 and I830. Comparing with FTIR spectra reported in literature, our samples resemble the CN thin-films obtained by Kouvetkakis [22] using thermal decomposition of triazine based compounds, the paracyanogen reported by Maya [31] or the "pseudo-carbon nitrides" by Komatsu [23]. Probably, the highest resemblance on FTIR terms found in literature is for spectra reported on porous carbon nitride frameworks obtained after pyrolysis of covalent triazine networks at high temperature 700 °C [25] but not from pyrolysis of triazine based compounds at low temperature < 400 °C [13]. In contrast, our chars are different compared with the guanidinium based chars from Rangel because absence of the 1650 and sharp 800 cm^{-1} peak absorption [32]. Guanidinium is the building block most similar to formamidinium with the difference of three $–NH_2$ groups instead of two surrounding the sp^2 carbon atom. This atomic bonding connectivity difference has a major impact on the type of carbon nitride formed (Section 4 Discussion).

Instead, the similarity of our chars to carbon nitrides obtained from pyrolysis of triazine-based precursors is reasonable as thermal decomposition of formamidinium yields into sym-triazine molecules [10]. In any case, there are significant differences depending on the synthesis temperature but the halide present in the precursor does not seem to have an influence on the final FTIR spectra. The analysis of deconvoluted FTIR peaks in the skeletal mixed modes indicates that, independently of halide precursor, the 830 °C sample increased the ~1150 cm^{-1} intensity peak by ~3.5 times compared to 630 °C sample. In contrast, ~1370 and ~1525 cm^{-1} peaks decreased ~50% and ~40%, respectively (Fig. S8 and Table S1). Tentatively, we ascribe these intensity peak changes to increased depletion of C_3N_3 triazine aromatic ring because of the higher pyrolysis temperature producing further condensation or bonding with other rings or plain thermal decomposition.

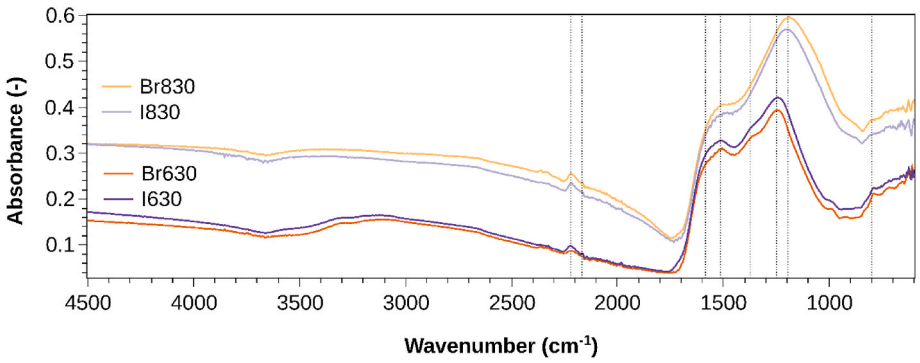

Fig. 3. FTIR raw spectra of the pure four samples recorded at room temperature and without baseline correction. Dot lines placed on 2220, 2167, 1584, 1516, 1373, 1250, 1195 and 800 cm^{-1}.

Table 4
Summary of FTIR peaks description.

Peak Assignment[a]		Absorption Intensity	
Wavenumber (cm^{-1})	Functional group	630 °C	830 °C
3600–3200	N – H stretching	weak	negligible
2220	C_{sp} – N_{sp}, stretching of nitrile group in aromatic ring	medium	medium
2170	N=C=O, isocyanate stretching	weak	weak
1600–1500	Skeletal Csp2 – Csp2 and Csp2 – Nsp2 mixed modes region	strong	strong
1370	"	weak	negligible
1250	"	strong	weak
1200	"	weak	strong
800	Triazine ring breathing	weak	negligible

[a] Peak assignment values have been rounded to the nearest tens. The setting of the exact position of the maximum and integrated peak intensity is reported in the supplementary information (Fig. S8 and Table S1).

3.5. Raman spectroscopy

In contrast with FTIR spectra, Raman spectra do not show obvious differences depending on temperature of pyrolysis for the samples (Fig. 4).

According to laser wavelength excitation, the 488 (785) nm excited Raman spectra show three (two) major peaks around ~1360 (~1325), ~1560 (~1550) and ~2825 cm^{-1}, see Fig. 4.a (Fig. 4.b). Raman spectra excited with 785 nm near-IR photons resemble better the FTIR spectra because both techniques are probing similar sp^2 structures [29,33]. In contrast, Raman spectra using 488 nm visible excitation (Fig. 4.a) are richer in features as: 1) A1 = 690 cm^{-1} and A2 = 990 cm^{-1} bands assigned to specific breathing modes of the C_3N_3 triazine ring [34], 2) ~2220 cm^{-1} band due to CN sp^1 vibration, 3) ~2825 cm^{-1} shoulder peak as the D2 second-order overtone [25,35,36], and 4) lack of bands corresponding to sp^3 hybridization in the synthesized materials. The ~1360 (~1325) cm^{-1} band accounts breathing modes ascribed uniquely to sp^2 six fold C=N rings (D band). Instead, the ~1560(~1550) cm^{-1} band corresponds to stretching modes for all type of sp^2 bonds including rings and polymeric chains (G band). Noteworthy, 1) G peak maximum position, 2) G dispersion (~0.03 cm^{-1}/nm), 3) full width at half maximum (FWHM) of G and 4) I_D/I_G ratio values agree with the high 40–45 at% N content in these CN materials [29]. Furthermore, the upshift of the G peak and its decreased FWHM following the increase of pyrolysis temperature agrees with the loss of N content observed by chemical bulk analysis and crystalline nanodomain thinning (sample amorphization) observed by X-ray analysis, respectively [29]. In the same way, the I_D/I_G ratio increases as pyrolysis temperature increases independently of the laser excitation (Table 5) but better observed for 488 nm excitation.

The increasing I_D/I_G ratio has to be associated to the condensation of triazine rings with temperature, since A1 and A2 breathing modes of triazine decreased (Fig. 4.a). Thus, some C–C bonds form, which can be

Table 5
Area ratio between D and G Raman peaks depending on photon excitation and pyrolysis temperature. Peak fittings and deconvolution reported in SI file (Figs. S9 and S10 and Tables S2 and S3).

Sample	Br630	I630	Br830	I830
I_D/I_G (488 nm)	2.17	2.14	2.79	2.50
I_D/I_G (785 nm)	2.98	3.11	4.18	3.27

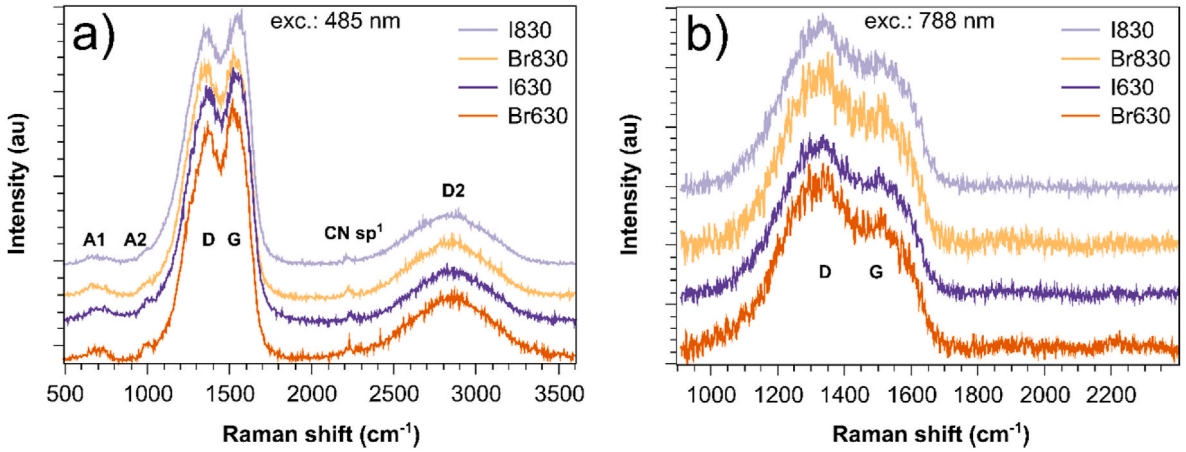

Fig. 4. Raman spectra of samples for a) 488 nm and b) 785 nm wavelength laser excitation.

chemically conjugated to surviving N–C ring bonds. However, an extended carbon network is still not possible even at the treatment temperature of 830 °C. This fact is in good agreement with the absence of any substantial development of the Raman G band and FTIR bands around 1580 cm-1. The I_D/I_G ratio of our samples is twice compared to those obtained from pyrolysis of covalent triazine framework [25,37], indicating that the presence of conjugated C–C–N sequences is higher pyrolyzing formamidinium precursors (a triazine-preserving event [10]) than directly triazine networks (a triazine-destruction event). The cluster size calculated using the Ferrari and Robertson equation $Lc = [(I_D/I_G)/0.0055]^{0.5}$ and I_D/I_G (485 nm) for Br630 and I630 low temperature samples is ~20 Å both. Instead, the Tuinstra-Koening expression for high temperature samples $Lc = 44(I_D/I_G)^{-1}$ indicates 16 and 18 Å for Br830 and I830, respectively, in good accordance with a condensation process and with the crystallite size obtained from the Scherrer equation. Finally, this high I_D/I_G also indicates a low band gap for the samples [27,29] as measured from UV–Vis absorption and discussed in the next section.

3.6. UV–vis spectroscopy

In contrast with yellow, red or brown powders obtained for conventional C_3N_4 type carbon nitrides [38], these black samples absorb all the visible and IR photon at least to 2500 nm wavelength (Fig. 5a). We found that high temperature samples show higher absorbance for photons above 1400 nm but there is no relevant difference in UV–Vis spectra considering the halide in precursor. Measuring optical properties in amorphous carbon and related materials is challenging [39]. It is important to remark that a conventional photomultiplier tube detector (200–900 nm) in the UV–Vis equipment would have measured both high and low temperature materials with nearly identical UV–Vis absorption spectrum. The pseudo absorption F(R∞) of these materials calculated using the reflectance data and Kubelka-Munk transformation determined a Tauc plot profile (Fig. 5b). The extrapolation of the Tauc profile estimates a Tauc gap as small as ~ +300 meV for 630 °C samples and ~ −300 meV for 830 °C samples. These low or even negative band gaps agree well with the high Raman I_D/I_G ratios empirically observed [29] and discussed in the before section. More conventional yellowish CNs present a band gap energy range between 2.5 and 2.8 eV due to π→π* transitions but as condensation increases and terminal amine groups are lost, the structure adopts a conformation in which electrons coming from nitrogen atoms can undergo the previous forbidden n→π* transition. As a consequence of this reduction of the band gap, these species adopt a dark brown color. Otherwise, the disordered structures show a black color like the graphite analogs [4,5].

Negative and indirect band gap indicates semimetal character for samples Br830 and I830. Recent first principles studies have predicted this semimetal behavior within C:N > 1 ratio carbon nitrides and chemical formula C_6N, C_9N_4 C_7N_6 and $C_{10}N_3$ [40–42]. A first attempt to measure photoluminescence in the raw solid samples obtained gave negative or negligible signal.

3.7. UPS spectroscopy

UPS and XPS valence band spectra determined absolute band energy edges in these samples (Fig. 6). The UPS spectral shape for the valence band maximum (VBM) zone is featureless and smooth in shape corresponding to amorphous carbon nitride materials (inset of Fig. 6.a) [24,43]. The 2p orbitals of sp^2 N and C atoms mainly constitute the occupied states near the energy gap [44]. The position of the valence-band maximum with reference to the Fermi level of the instrument (VBM_F) is determined by the extrapolation of the steepest descent of the leading edge of the spectrum to the base line. In this case, there is different binding energy onset depending on halide precursors for low temperature pyrolysis samples Br630 (~2 eV) and I630 (~1 eV). In contrast, high temperature Br830 and I830 samples have the VBM_F in the 0 eV Fermi level. The secondary electron cut off (SECO) zone grouped both high and low temperature samples with onset over 18.2 eV (16.6 eV) for Br630 and I630 (Br830 and I830). Then, the absolute VBM with reference to vacuum level is $VBM = SECO - h\nu - VBM_F = -5.0$ eV for Br630, -4.0 eV for I630 and -4.6 eV for Br830 and I830. Fig. 7 depicts tentatively a scheme of the band energy levels for the samples. The optical band gap from Tauc plots determined the conduction band minimum (CBM) by subtraction to VBM. In contrast with wide band gap conventional graphite like C_3N_4 or melon type polymers whose CBM and VBM energy levels align well for the standard potential of proton reduction reaction (−4.44 eV) and water oxidation (−5.67 eV), these samples are narrow band gap with CBM ideally aligned for proton reduction in the case of I630. Instead, Br630/Br830/I830 samples VBM level complies for hole (positive charge carrier) selective extraction material in perovskite solar cells (VBM ~ −5.4 eV).

Despite the featureless UPS valence band spectra, the XPS data of the valence band zone (Fig. 6.b) show a common feature for all samples leading shoulder at the top of the valence band near 4 eV for 2p-π contributions and another peak at around 6 eV. Latter is only visible for high temperature samples suggesting an increased degree of

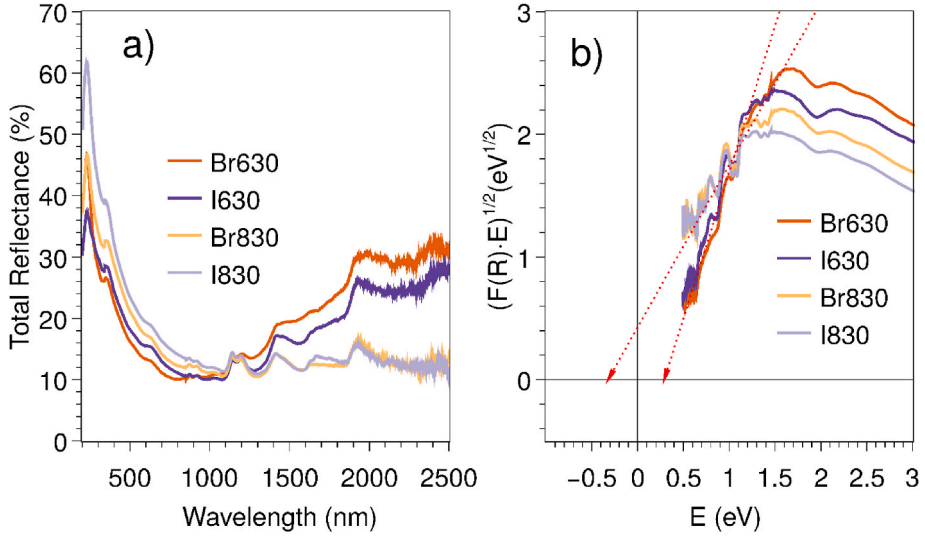

Fig. 5. a) UV–vis total (specular or direct plus diffuse) reflectance of samples and b) Tauc plot (indirect allowed band gap setting) of the Kubelka-Munk transformation of the total reflectance data. Red arrow indicates the band gaps after extrapolation to zero axis.

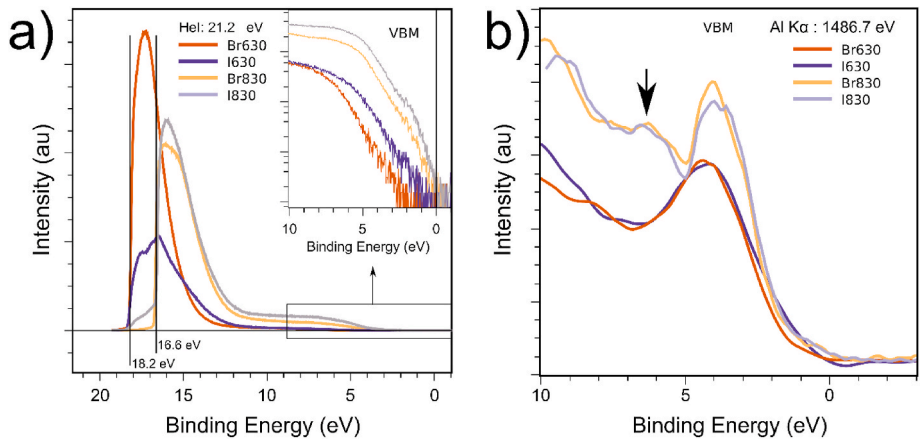

Fig. 6. a) UPS of the four samples measured with the 21.2 eV excitation energy corresponding to He I radiation. Inset: valence band spectra. b) XPS valence band spectra of the four samples measured with the 1486.7eV excitation energy corresponding to Al Kα radiation. The zero of energy is the Fermi level.

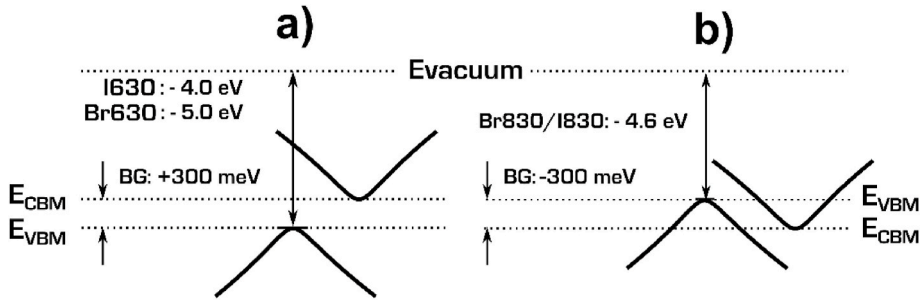

Fig. 7. Scheme depicting band structure and alignments in absolute scale (vacuum level) considering intrinsic indirect band gap (BG) type obtained from UV–Vis-IR spectrometry and Tauc plots. VBM energy level from UPS data for a) Br630 and I630 and b) semimetals Br830 and I830.

crosslinking/condensation due to 2p-σ contributions [43].

3.8. High resolution XPS spectroscopy

High resolution XPS data from C 1s and N 1s core levels disclose the local structural environment of these atoms in the samples (data from survey spectra were included in section 3.1 for chemical composition analysis). Deconvoluted C 1s spectra peaks show two peaks of similar area at binding energies of ~284.2 and ~285.5 eV for all samples corresponding to unsaturated C_{sp2}-C_{sp2} (and/or C_{sp2}-H) and N_{sp2}-(C_{sp2}-H)-N_{sp2} (triazine ring), respectively (Fig. S5). There is no clear distinction on the C 1s pattern depending on halide precursor used to obtain the material but high pyrolysis temperature samples show an increased area for the 284.2 eV peak. It indicates correlation between N atom content loss and increased conjugation of the material samples at high temperature synthesis. However, it is not possible to know in absolute terms the quantity of decreased/increased triazine domain because the unknown true contribution of adventitious carbon to the 285.5C 1s peak area. Remarkably, the absence of ~288 eV peak corresponding to C_{sp2}-$(N_{sp2})_3$ indicates absence of heptazine units in these materials. [24,44,45].

The N 1s zone offers more clear insight about the chemical environment surrounding the N atom depending on sample (Fig. 8). Deconvoluted N 1s spectra show three peaks at 397.9, 399.1, 400.2 and small shoulder at 402.5 eV corresponding to pyridinic (C_{sp2}-N_{sp2}-C_{sp2}) or sym-triazine ring, pyrrolic (C-N_{sp2}-H), tricoordinated quaternary N^+ (N^+_{sp3}-(C_{sp2})$_3$) and oxidized NO, respectively [3,46]. As before C 1s zone, there is no clear distinction for N 1s pattern depending on halide, but pyrrolic area showed a decreased area in 399.1 eV peak and increased area in 400.2 eV for high temperature samples. It indicated correlation between H atom content loss from pyrrolic moiety and an increased full condensation as tricoordinated quaternary N atom in the material samples obtained at high temperature pyrolysis. Furthermore, the oxidized N content also increased for high temperature samples.

3.9. SEM

SEM images obtained at different magnifications show that samples consist of a bunch of micron-size randomly oriented wrinkled sheets (Fig. 9, Fig. S11).

The material has amorphous arrangement at the microscale, in agreement with XRD (Section 3.3), even inside relatively large aggregate particles. Electron diffraction from TEM confirmed this result (Section 3.10 below). Despite this furry aspect of samples, the textural properties did not show significant adsorption area (Section 3.2). Under our understanding, there is no clear morphological distinction from SEM images between samples obtained using different halide precursor or even obtained at different temperature. However, the EDS chemical analysis from SEM (Section 3.1) showed compositional differences depending on pyrolysis temperature.

3.10. STEM

High/low-magnification TEM images of the samples show large amorphous flakes (Fig. 10) confirmed by selected area electron diffraction (SAED) (inset Fig. 10a–d) consisting of two diffuse large rings at ~1.85 and ~1.05 Å d-spacing which attest of nanocrystalline or amorphous structure.

TEM micrographs and SAED indicate no clear morphological distinction between samples obtained using different halide precursor or pyrolysis temperature. However, the EDS chemical analysis from TEM equipment (Section 3.1) showed compositional differences depending on pyrolysis temperature.

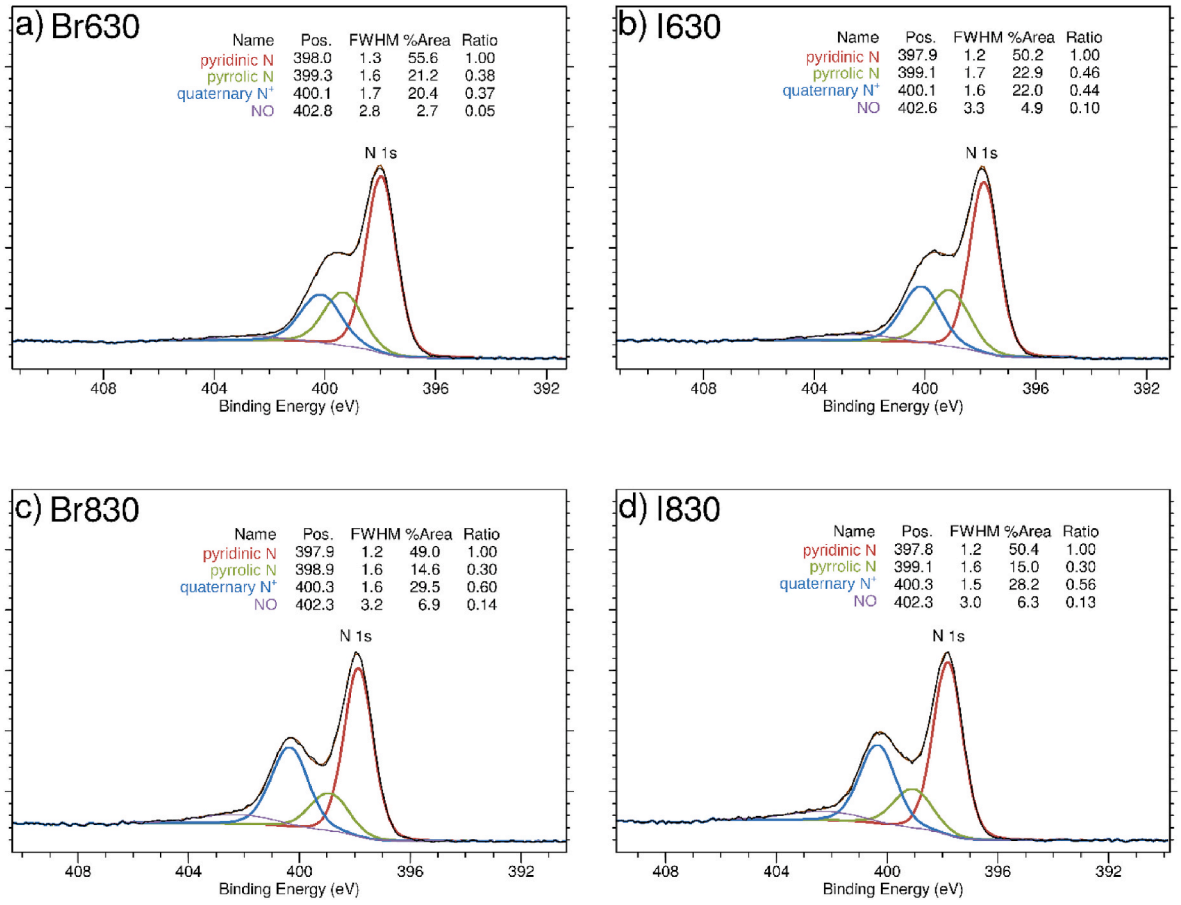

Fig. 8. Deconvolution of the N1s XPS spectra of a) Br630, b) I630, c) Br830 and d) I830 samples.

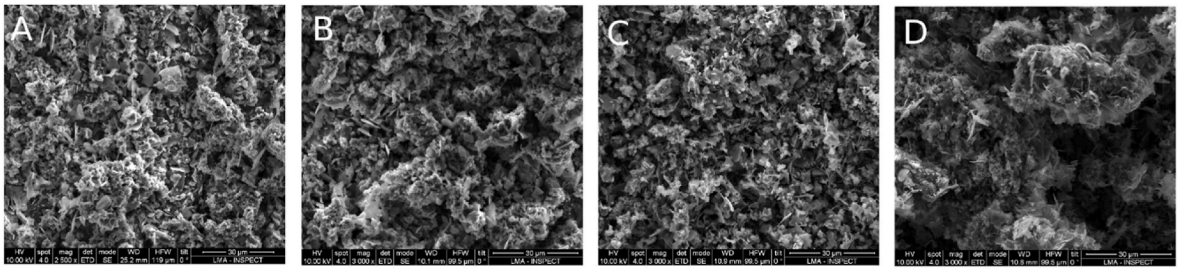

Fig. 9. SEMs images of a) Br630, b) I630, c) Br830 and d) I830.

3.11. NMR

^{13}C-MAS-NMR spectra show that samples have a broad asymmetric resonance at ~150 ppm attributed to sp^2 C–N or C-atoms of heterocyclic compounds containing N (Fig. 11) [47]. Triazine based graphitic carbon nitrides show this resonance [30]. The asymmetry of the main peak is attributed to the existence of resonance band at 110–120 ppm range due to 1) contribution of terminal sp CN [13,31] and 2) Csp^2-Csp^2 environment [47]. Latter contribution increased in samples Br830 and I830 correlating with the loss of N and larger conjugation of high temperature pyrolysis samples.

3.12. Electronic conductivity

The resistivity of samples becomes constant independently of the applied voltage applying pressure $\geq$ 57.0 MPa (Table 6, Fig. S2). Then, inner grain material assumes the electronic conductivity value discarding influence of other factors such as grain shape, electron percolation pathway, number and area of current conducting intergranular contacts and surface layers [48].

The electric conductivity of the two samples pyrolized at 830 °C is two orders of magnitude higher than the corresponding samples pyrolyzed at 630 °C. Besides, the chars obtained from iodide precursor show an order of magnitude higher in conductivity that the corresponding chars obtained from Br precursor. This result suggests that more extended and interconnected conductive domains are formed in the chars obtained from higher pyrolysis temperature, but it is unclear the difference observed depending on precursor. We hypothesized that I_2 and Br_2 molecule size and sublimation temperature play a relevant role in the formation of the amorphous CN network at early (low temperature) stages. On the other hand, Raman and high resolution XPS spectra (Section 3.5 and 3.8) detect an increase of six fold ring aromaticity or more conjugated nanodomains on samples pyrolyzed at higher temperatures explaining the improvement of conductivity in these samples

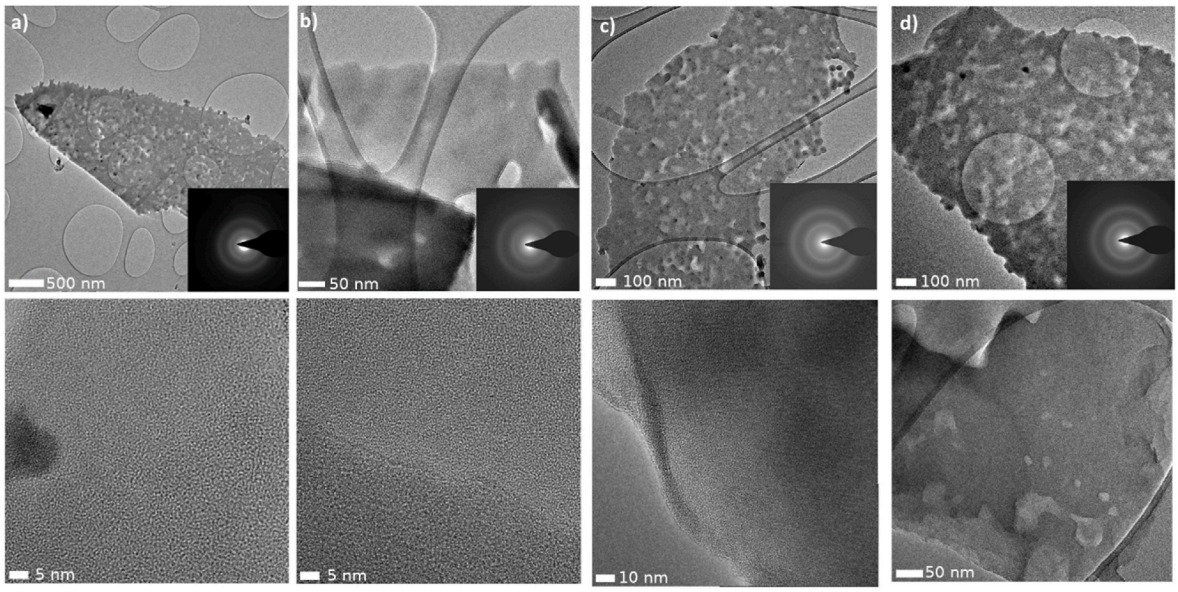

Fig. 10. TEM images and SAED as inset of samples a) Br630, b) I630, c) Br830 and d) I830.

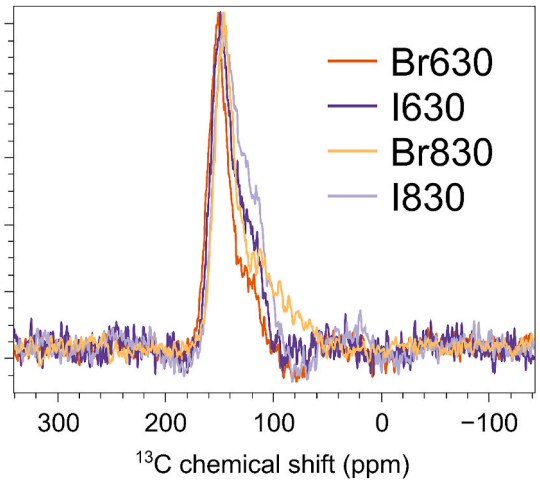

Fig. 11. ^{13}C-MAS-NMR of the samples.

Table 6
Conductivity of the samples measured by electric impedance spectroscopy at 1 V of voltage bias and 115 MPa of pressure.

Sample	Br630	I630	Br830	I830
σ (ohm·cm)$^{-1}$	$6.1{\cdot}10^{-6}$	$1.0{\cdot}10^{-5}$	$1.1{\cdot}10^{-4}$	$7.2{\cdot}10^{-3}$

and the change from semiconductor to semimetallic character (Section 3.7, Fig. 7).

4. Discussion

4.1. Mechanism of formation of triazine based amorphous carbon nitrides (TACN)

The key molecule in the synthetic route for extended CN materials is melamine [2]. Melamine is a trimer of cyanamide with triazine ring skeleton and 1,3,5- carbon position atoms terminated in –NH_2. Conventional CN precursors reaching melamine intermediate during pyrolysis include cyanamide, dicyanamide, urea, thiourea, cyanide, thiocyanate, guanidinium and dicyanamide salts. Instead, our CN precursor is the formamidinium cation, or more specifically, its conjugated base formamidine (Scheme 1.a). Formamidine has the special ability to polymerize with itself sequentially until linear trimer set (Scheme 1.b), then a cyclization reaction on the trimer forms the stable six units ring *sym*-triazine (Scheme 1.b.1) [10,49]. This *sym*-triazine is the key molecule in the synthetic route of TACN. In essence, the carbon atom in melamine is surrounded by three N atoms and this atomic connectivity remains for all known synthesis pathways of extended CN based on triazine or heptazine units [2,3]. Instead, *sym*-triazine with 1,3,5- carbon position terminated in acidic –H provides three different reactivity points for condensation reaction non-existent in melamine.

We think that at early stages of TACN formation, formamidine grows simultaneously *sym*-triazine (Scheme 1.b.1) and short oligomers of poly-HCN (H–$(N{=}CH)_n$–NH_2) (Scheme 1.b.2). If only full sym-triazine was formed, the char would not be found because of the early sublimation and leakage from the reaction zone of the white powder *sym*-triazine (sublimation at ~80 °C). On the other hand, full linear poly-HCN formation does not match Raman and FTIR spectra signature [34] and chemical analysis composition indicates low hydrogen content (Section 3.1). Therefore, we rule out that one chemical pathway manifests prevalently. Then, early condensation of *sym*-triazine units with itself and with HCN oligomers might take place following the reaction network depicted in Scheme 1.c-g: 1) C–C bond formation after condensation of –NH_2 in HCN oligomer and –CH from *sym*-triazine releasing NH_3 (Scheme 1.c), 2) C–N bond formation after condensation of = NH in HCN oligomer and –CH from *sym*-triazine releasing H_2 (Scheme 1.d), 3) ring linkage by condensation of –CH from two *sym*-triazines releasing H_2 (Scheme 1.e) and 4) C–C bond formation after HCN release (Scheme 1.f). The product of reaction depicted in Scheme 1.f would be a good atomic model representation of TACN where wavy bond means C–C bonding between *sym*-triazine rings, C–N or C–C bond to HCN oligomers or nitrile group (Scheme 1.g).

This proposed self-polymerization mechanism agrees with observed chemical composition analysis of the carbon nitride chars obtained at two different temperature runs. The starting precursor formamidine (CN_2H_4) releases continuously large amounts of NH_3 and H_2 to reach the final $CN_{0.85}H_{0.04}$ and $CN_{0.65}H_{0.02}$ chemical composition in Br630(I630) and Br830(I830), respectively. In our opinion, there would be no abrupt difference in chemical composition or functional groups between Br630 (I630) and Br830(I830) samples. This is a continuum degassing process of the initial char where the Br830(I830) sample ends up at 200 °C

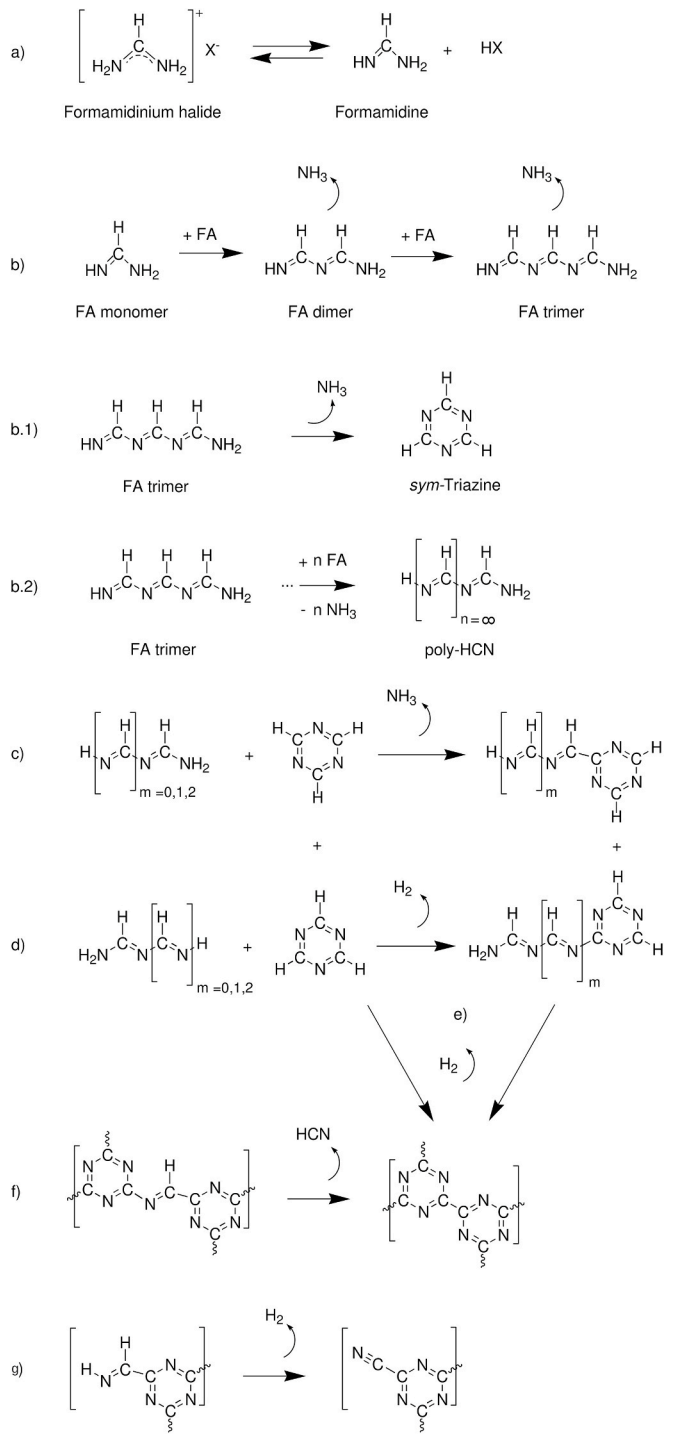

Scheme 1. Proposed self-polymerization mechanism of FA to form TACN.

higher in temperature than Br630(I630) type sample. Consequently, Br830(I830) spent 25% more time in the furnace than Br630(I630) (constant heating temperature ramp is 20 °C/min for both samples). Then, the temperature-dependent difference observed in chemical composition between Br630(I630) and Br830(I830) can be mainly attributed to the greater rate (or yield) of 1.c to 1.f pathways set in Scheme 1 at higher temperature favoring the release of volatiles NH_3, H_2 and HCN.

Noteworthy, the nitrogen content is high to consider TACN as nitrogen-doped carbons [3]. The small amount of hydrogen remaining is = NH or –NH_2 but no –CH from *sym*-triazine (section 3.4 FTIR spectroscopy). Overall, the analysis of the spectra versus annealing temperature reveals that the major differences are microstructure changes and reorganization at atomic scale of C–N and C–C configurations. Halide anion (Br^- and I^-) evolved at early low temperature as hydrogen halide gas (HI and HBr boiling point is −35.4 °C and −66 °C, respectively) noting the negligible effect of the precursor halide on the final pyrolysis product. A lower mass yield for high pyrolysis temperature chars (Section 2.1) indicates a material loss including HCN release favoring the spatial approximation of aromatic rings and conjugation that improves the electric conductivity (Scheme 1.f). Released gas components stated in this proposed self-polymerization mechanism, specifically HCN, were observed during previous TG-MS experiments in FAI and FABr [10]. Although the material is amorphous (SAED), the interplanar distance of the condensed triazine rings in π−π stacking originates the XRD broad peak (Section 3.3).

We found in the scientific literature a great similarity in terms of chemical signature in FTIR, Raman and XPS spectroscopy with porous carbon nitride frameworks derived from pyrolysis of covalent triazine frameworks [25]. In contrast to these compounds, our material is not porous but amorphous and compact, ideal for developing chemically inert protective coatings. Noteworthy, formamidine molecule is not limited to bulk pyrolysis methods but it could be envisaged as precursor for a vapor-phase transport assisted direct condensation method to prepare carbon nitride films with controllable thickness [50].

4.2. Perovskite solar cells

In contrast with FA^+, methylammonium cation (MA^+), the second most commonly used cation in the field of hybrid halide perovskite semiconductors [51], does not produce carbon nitrides after pyrolysis [52]. Because both low molecular weight organic cations have similar thermal evaporation temperatures [53], the ability of FA^+ to polymerize with itself is due to the sp^2 hybridized C and N atoms in contrast to the lower chemical potential of C and N as sp^3 atoms in MA^+. Nowadays, the most efficient and most stable hybrid perovskite based solar cells contain > 85% formamidinium cation or larger amount in the A position of the perovskite structure being the remainder inorganic cesium cation followed by methylammonium cation if any [53]. Therefore, this finding of FA salts forming bulk carbon nitride by thermal decomposition opens the door to a new strategy to improve operational stability in perovskite solar cells: sacrificing part of the active perovskite thin film to natively form a protective CN layer in a manner equivalent to the passivation role of SiO_2 natively generated in Si solar cells [54]. In our opinion, it could be the first stone on the path to get stable and commercial hybrid perovskite solar cells. But it remains to be demonstrated that a CN based native passivation film can be partially formed on perovskite and the remaining active layer could still be functional in photovoltaic cells, LEDs and battery electrode applications.

5. Conclusions

Formamidinium halide salts pyrolysis led to amorphous and non-porous products that cannot be considered neither conventional carbon (IV) nitrides nor N doped carbon materials. Instead, they are chemically tunable carbon nitrides ($C_xN_yH_z$) composed by sp^2 six member rings and short unsaturated oligomers of poly-HCN conjugated domains. Heptazine type moiety is not detected in FTIR nor high resolution XPS C1s spectra, therefore we conclude that conjugated domains present in the synthesized samples are triazine or triazine-like structures. The halide used in the initial precursor leads to negligible differences in the carbon nitride product obtained. On the other hand, pyrolysis temperature plays a much more relevant role since samples synthesized at 830 °C present a lower nitrogen content, a higher degree of conjugation, a smaller crystallite size and a higher electronic conductivity. Regarding their potential applications, hybrid perovskites are of the outmost studied photovoltaic material in the last decade, being

the formamidinium cation one of the most used *A* type cation in hybrid halogenated perovskite structure. A selective and controlled thermal degradation of the outer exposed thin-film of formamidinium based perovskite could be employed simultaneously as hole selective extraction layer and promising inert native passivation layer against environmental agents in perovskite solar cells.

CRediT authorship contribution statement

E.J.J-P conceived the idea, designed experiments and supervised the work. M.H. designed experiments, supervised the work, performed and analysed conductivity measurements.I.C-R. wrote initial version of the manuscript, performed TACN preparation, UV-vis-IR and conductivity measurements.N.N. carried out adsorption isotherms, X-ray diffraction and Raman spectroscopy. F.D. prepared and characterized FAI and FABr precursors.R.A. supervised C.F. and they performed and analyzed TEM, EELS and EDS (TEM equipment)A.A-C performed X-ray, adsorption isotherms and XPS.All authors contributed to editing the paper.

Declaration of competing interest

The authors declare that they have no known competing financial interests or personal relationships that could have appeared to influence the work reported in this paper.

Acknowledgements

E.J.J-P acknowledges the funding support from MCIN/AEI/10.13039/501100011033 and European Union NextGenerationEU/PRTR (project grants PID2019-107893RB-I00 and EIN2020-112315, respectively). M.H. acknowledges the funding support from MCIN/AEI/10.13039/501100011033 for the Ramón y Cajal fellowship (RYC-2018-025222-I) and the project PID2019-108247RA-I00. R.A. acknowledges funding from the Spanish MICINN (project grant PID2019-104739 GB-100/AEI/10.13039/501100011033). RA also acknowledge to Government of Aragon (project DGA E13-20R (FEDER, EU)) and European Union H2020 program “ESTEEM3” (823717). A.A-C acknowledges financial support from Spanish MCIN/AEI/10.13039/501100011033 under project PID2019-104272RB-C51/AEI/10.13039/501100011033 and the Diputación General de Aragón under project T03_20R (Grupo Reconocido). Authors would like to acknowledge the use of Servicio General de Apoyo a la Investigación-SAI, Universidad de Zaragoza. The SEM and TEM measurements were performed in the Laboratorio de Microscopias Avanzadas (LMA) at the Universidad de Zaragoza (Spain). The synthesis of the materials has been performed at the facilities of the Nanoparticle Synthesis Unit 9 of CIBER-BBN ICTS NANBIOSIS.

Appendix A. Supplementary data

Supplementary data to this article can be found online at https://doi.org/10.1016/j.carbon.2022.05.051.

References

[1] E. Kroke, M. Schwarz, Novel group 14 nitrides, Coord. Chem. Rev. 248 (5–6) (2004) 493–532, https://doi.org/10.1016/j.ccr.2004.02.001.
[2] F.K. Kessler, Y. Zheng, D. Schwarz, C. Merschjann, W. Schnick, X. Wang, M. J. Bojdys, Functional carbon nitride materials design strategies for electrochemical devices, Nat. Rev. Mater. 2 (6) (2017), 17030, https://doi.org/10.1038/natrevmats.2017.30.
[3] T.S. Miller, A.B. Jorge, T.M. Suter, A. Sella, F. Corà, P.F. McMillan, Carbon nitrides: synthesis and characterization of a new class of functional materials, Phys. Chem. Chem. Phys. 19 (24) (2017) 15613–15638, https://doi.org/10.1039/c7cp02711g.
[4] J.R. Holst, E.G. Gillan, From triazines to heptazines: deciphering the local structure of amorphous nitrogen-rich carbon nitride materials, J. Am. Chem. Soc. 130 (23) (2008) 7373–7379, https://doi.org/10.1021/ja709992s.
[5] Y. Xu, S.-P. Gao, Band gap of C_3N_4 in the GW approximation, Int. J. Hydrogen Energy 37 (15) (2012) 11072–11080, https://doi.org/10.1016/j.ijhydene.2012.04.138.
[6] A. Wang, C. Wang, L. Fu, W. Wong-Ng, Y. Lan, Recent advances of graphitic carbon nitride-based structures and applications in catalyst, sensing, imaging, and LEDs, Nano-Micro Lett. 9 (4) (2017) 1–21, https://doi.org/10.1007/s40820-017-0148-2.
[7] M.A. Green, A. Ho-Baillie, H.J. Snaith, The emergence of perovskite solar cells, Nat. Photonics 8 (7) (2014) 506–514, https://doi.org/10.1038/nphoton.2014.134.
[8] Y. Rong, Y. Hu, A. Mei, H. Tan, M.I. Saidaminov, S.I. Seok, M.D. McGehee, E. H. Sargent, H. Han, Challenges for commercializing perovskite solar cells, Science 361 (6408) (2018) 1214, https://doi.org/10.1126/science.aat8235.
[9] E.J. Juarez-Perez, M. Haro, Perovskite solar cells take a step forward, Science 368 (2020) 1309, https://doi.org/10.1126/science.abc5401.
[10] E.J. Juarez-Perez, L.K. Ono, Y. Qi, Thermal degradation of formamidinium based lead halide perovskites into sym-triazine and hydrogen cyanide observed by coupled thermogravimetry - mass spectrometry analysis, J. Mater. Chem. 7 (2019) 16912–16919, https://doi.org/10.1039/c9ta06058h.
[11] E. Ech-Chamikh, A. Essafti, Y. Ijdiyaou, M. Azizan, XPS study of amorphous carbon nitride (aC:N) thin films deposited by reactive RF sputtering, Sol. Energy Mater. Sol. Cells 90 (10) (2006) 1420–1423, https://doi.org/10.1016/j.solmat.2005.10.007.
[12] C. Pérez-Fernández, M. Ruiz-Bermejo, S. Gálvez-Martínez, E. Mateo-Martí, An XPS study of HCN-derived films on pyrite surfaces: a prebiotic chemistry standpoint towards the development of protective coatings, RSC Adv. 11 (33) (2021) 20109–20117, https://doi.org/10.1039/d1ra02658e.
[13] V.N. Khabashesku, J.L. Zimmerman, J.L. Margrave, Powder synthesis and characterization of amorphous carbon nitride, Chem. Mater. 12 (11) (2000) 3264–3270, https://doi.org/10.1021/cm000328r.
[14] R.F. Egerton, Electron Energy-Loss Spectroscopy in the Electron Microscope, third ed. ed., Springer, New York, 2011.
[15] L. Lajaunie, C. Pardanaud, C. Martin, P. Puech, C. Hu, M.J. Biggs, R. Arenal, Advanced spectroscopic analyses on a:CH materials: revisiting the EELS characterization and its coupling with multi-wavelength Raman spectroscopy, Carbon 112 (2017) 149–161, https://doi.org/10.1016/j.carbon.2016.10.092.
[16] A.C.Y. Liu, R. Arenal, D.J. Miller, X. Chen, J.A. Johnson, O.L. Eryilmaz, A. Erdemir, J.B. Woodford, Structural order in near-frictionless hydrogenated diamondlike carbon films probed at three length scales via transmission electron microscopy, Phys. Rev. B 75 (2007), 205402, https://doi.org/10.1103/PhysRevB.75.205402.
[17] A.C. Ferrari, A. Libassi, B.K. Tanner, V. Stolojan, J. Yuan, L.M. Brown, S.E. Rodil, B. Kleinsorge, J. Robertson, Density, sp^3 fraction, and cross-sectional structure of amorphous carbon films determined by X-ray reflectivity and electron energy-loss spectroscopy, Phys. Rev. B 62 (16) (2000), 11089, https://doi.org/10.1103/PhysRevB.62.11089.
[18] S. Hettler, D. Sebastian, M. Pelaez-Fernandez, A.M. Benito, W.K. Maser, R. Arenal, In-situ reduction by Joule heating and measurement of electrical conductivity of graphene oxide in a transmission electron microscope, 2D Mater. 8 (3) (2021), 031001, https://doi.org/10.1088/2053-1583/abedc9.
[19] M. Pelaez-Fernandez, A. Bermejo, A.M. Benito, W.K. Maser, R. Arenal, Detailed thermal reduction analyses of Graphene Oxide via in-situ TEM/EELS studies, Carbon 178 (2021) 477–487, https://doi.org/10.1016/j.carbon.2021.03.018.
[20] J. Sánchez-González, A. Macas-Garca, M.F. Alexandre-Franco, V. Gómez-Serrano, Electrical conductivity of carbon blacks under compression, Carbon 43 (4) (2005) 741–747, https://doi.org/10.1016/j.carbon.2004.10.045.
[21] T. Suter, V. Brázdová, K. McColl, T.S. Miller, H. Nagashima, E. Salvadori, A. Sella, C.A. Howard, C.W. Kay, F. Corà, others, Synthesis, structure and electronic properties of graphitic carbon nitride films, J. Phys. Chem. C 122 (44) (2018) 25183–25194, https://doi.org/10.1021/acs.jpcc.8b07972.
[22] J. Kouvetakis, M. Todd, B. Wilkens, A. Bandari, N. Cave, Novel synthetic routes to carbon-nitrogen thin films, Chem. Mater. 6 (6) (1994) 811–814, https://doi.org/10.1021/cm00042a018.
[23] T. Komatsu, T. Nakamura, Polycondensation/pyrolysis of tris-s-triazine derivatives leading to graphite-like carbon nitrides, J. Mater. Chem. 11 (2) (2001) 474–478, https://doi.org/10.1039/b005982j.
[24] Y. Kang, Y. Yang, L.-C. Yin, X. Kang, G. Liu, H.-M. Cheng, An amorphous carbon nitride photocatalyst with greatly extended visible-light-responsive range for photocatalytic hydrogen generation, Adv. Mater. 27 (31) (2015) 4572–4577, https://doi.org/10.1002/adma.201501939.
[25] X. Lan, Y. Li, C. Du, T. She, Q. Li, G. Bai, Porous carbon nitride frameworks derived from covalent triazine framework anchored Ag nanoparticles for catalytic CO_2 conversion, Chem. Eur J. 25 (36) (2019) 8560–8569, https://doi.org/10.1002/chem.201900563.
[26] S.Y. Chong, J.T.A. Jones, Y.Z. Khimyak, A.I. Cooper, A. Thomas, M. Antonietti, M. J. Bojdys, Tuning of gallery heights in a crystalline 2D carbon nitride network, J. Mater. Chem. 1 (4) (2013) 1102–1107, https://doi.org/10.1039/c2ta01068b.
[27] G. Fanchini, A. Tagliaferro, G. Messina, S. Santangelo, A. Paoletti, A. Tucciarone, Vibrational properties and microstructure of reactively sputtered hydrogenated carbon nitrides, J. Appl. Phys. 91 (3) (2002) 1155–1165, https://doi.org/10.1063/1.1425424.
[28] M. Lejeune, O. Durand-Drouhin, S. Charvet, A. Zeinert, M. Benlahsen, On the induced microstructure changes of the amorphous carbon nitride films during annealing, J. Appl. Phys. 101 (12) (2007), 123501, https://doi.org/10.1063/1.2747218.
[29] A.C. Ferrari, S.E. Rodil, J. Robertson, Interpretation of infrared and Raman spectra of amorphous carbon nitrides, Phys. Rev. B 67 (15) (2003), 155306, https://doi.org/10.1103/physrevb.67.155306.

[30] G. Algara-Siller, N. Severin, S.Y. Chong, T. Björkman, R.G. Palgrave, A. Laybourn, M. Antonietti, Y.Z. Khimyak, A.V. Krasheninnikov, J.P. Rabe, others, Triazine-based graphitic carbon nitride: a two-dimensional semiconductor, Angew. Chem. Int. Ed. 53 (29) (2014) 7450–7455, https://doi.org/10.1002/ange.201402191.
[31] L. Maya, Paracyanogen reexamined, J. Polym. Sci., Part A: Polym. Chem. 31 (10) (1993) 2595–2600, https://doi.org/10.1002/pola.1993.080311020.
[32] L.S. Rangel, J.R. de la Rosa, C.J.L. Ortiz, M.J. Castaldi, Pyrolysis of urea and guanidinium salts to be used as ammonia precursors for selective catalytic reduction of NO_x, J. Anal. Appl. Pyrolysis 113 (2015) 564–574, https://doi.org/10.1016/j.jaap.2015.04.007.
[33] S.E. Rodil, Infrared spectra of amorphous carbon based materials, Diam. Relat. Mater. 14 (8) (2005) 1262–1269, https://doi.org/10.1016/j.diamond.2005.01.044.
[34] E. Quirico, G. Montagnac, V. Lees, P.F. McMillan, C. Szopa, G. Cernogora, J.-N. Rouzaud, P. Simon, J.-M. Bernard, P. Coll, others, New experimental constraints on the composition and structure of tholins, Icarus 198 (1) (2008) 218–231, https://doi.org/10.1016/j.icarus.2008.07.012.
[35] P. Kumar, E. Vahidzadeh, U.K. Thakur, P. Kar, K.M. Alam, A. Goswami, N. Mahdi, K. Cui, G.M. Bernard, V.K. Michaelis, C.3N.5 others, A low bandgap semiconductor containing an azo-linked carbon nitride framework for photocatalytic, photovoltaic and adsorbent applications, J. Am. Chem. Soc. 141 (13) (2019) 5415–5436, https://doi.org/10.1016/j.diamond.2005.01.044.
[36] Á. García, M. Retuerto, C. Dominguez, L. Pascual, P. Ferrer, D. Gianolio, A. Serrano, P. Assmann, D.G. Sanchez, M.A. Pena, others, Fe doped porous triazine as efficient electrocatalysts for the oxygen reduction reaction in acid electrolyte, Appl. Catal., B 264 (2020), 118507, https://doi.org/10.1016/j.apcatb.2019.118507.
[37] S. Abednatanzi, P.G. Derakhshandeh, K. Leus, H. Vrielinck, F. Callens, J. Schmidt, A. Savateev, P. Van Der Voort, Metal-free activation of molecular oxygen by covalent triazine frameworks for selective aerobic oxidation, Sci. Adv. 6 (14) (2020), https://doi.org/10.1126/sciadv.aaz2310 eaaz2310.
[38] S. Ye, R. Wang, M.-Z. Wu, Y.-P. Yuan, A review on g-C_3N_4 for photocatalytic water splitting and CO_2 reduction, Appl. Surf. Sci. 358 (2015) 15–27, https://doi.org/10.1016/j.apsusc.2015.08.173.
[39] G.D. Gesesse, A. Gomis-Berenguer, M.-F. Barthe, C.O. Ania, On the analysis of diffuse reflectance measurements to estimate the optical properties of amorphous porous carbons and semiconductor/carbon catalysts, J. Photochem. Photobiol., A 398 (2020), 112622, https://doi.org/10.1016/j.jphotochem.2020.112622.
[40] B. Mortazavi, M. Shahrokhi, A.V. Shapeev, T. Rabczuk, X. Zhuang, Prediction of C_7N_6 and C_9N_4: stable and strong porous carbon-nitride nanosheets with attractive electronic and optical properties, J. Mater. Chem. C 7 (35) (2019) 10908–10917, https://doi.org/10.1039/C9TC03513C.
[41] A. Bafekry, M. Shahrokhi, A. Shafique, H.R. Jappor, F. Shojaei, S.A.H. Feghhi, M. Ghergherehchi, D. Gogova, Two-dimensional carbon nitride C_6N nanosheet with egg-comb-like structure and electronic properties of a semimetal, Nanotechnology 32 (21) (2021), 215702, https://doi.org/10.1088/1361-6528/abd50c.
[42] H. Chen, S. Zhang, W. Jiang, C. Zhang, H. Guo, Z. Liu, Z. Wang, F. Liu, X. Niu, Prediction of two-dimensional nodal-line semimetals in a carbon nitride covalent network, J. Mater. Chem. 6 (24) (2018) 11252–11259, https://doi.org/10.1039/c8ta02555j.
[43] A. Mansour, D. Ugolini, Photoelectron-spectroscopy study of amorphous a-CN_x:H, Phys. Rev. B 47 (16) (1993), 10201, https://doi.org/10.1103/PhysRevB.47.10201.
[44] K. Akaike, K. Aoyama, S. Dekubo, A. Onishi, K. Kanai, Characterizing electronic structure near the energy gap of graphitic carbon nitride based on rational interpretation of chemical analysis, Chem. Mater. 30 (7) (2018) 2341–2352, https://doi.org/10.1021/acs.chemmater.7b05316.
[45] T. Chen, W.-Q. Li, W.-B. Hu, W.-J. Hu, Y.A. Liu, H. Yang, K. Wen, Direct synthesis of covalent triazine-based frameworks (CTFs) through aromatic nucleophilic substitution reactions, RSC Adv. 9 (31) (2019) 18008–18012, https://doi.org/10.1039/c9ra02934f.
[46] D.Y. Osadchii, A.I. Olivos-Suarez, A.V. Bavykina, J. Gascon, Revisiting nitrogen species in covalent triazine frameworks, Langmuir 33 (50) (2017) 14278–14285, https://doi.org/10.1021/acs.langmuir.7b02929.
[47] M. Ruiz-Bermejo, J.L. de la Fuente, C. Rogero, C. Menor-Salván, S. Osuna-Esteban, J.A. Martín-Gago, New insights into the characterization of 'insoluble black HCN polymers, Chem. Biodivers. 9 (1) (2012) 25–40, https://doi.org/10.1002/cbdv.201100036.
[48] K.-J. Euler, R. Kirchhof, H. Metzendorf, The electric conductivity and related phenomena of compressed powder materials, Mater. Chem. 4 (4) (1979) 611–629, https://doi.org/10.1016/0390-6035(79)90076-2.
[49] F.C. Schaefer, I. Hechenbleikner, G.A. Peters, V.P. Wystrach, Synthesis of the sym-triazine system. I. Trimerization and cotrimerization of amidines, J. Am. Chem. Soc. 81 (6) (1959) 1466–1470, https://doi.org/10.1021/ja01515a046.
[50] Z. Liu, C. Wang, Z. Zhu, Q. Lou, C. Shen, Y. Chen, J. Sun, Y. Ye, J. Zang, L. Dong, C.-X. Shan, Wafer-scale growth of two-dimensional graphitic carbon nitride films, Matter 4 (5) (2021) 1625–1638, https://doi.org/10.1016/j.matt.2021.02.014.
[51] L.K. Ono, E.J. Juarez-Perez, Y. Qi, Progress on perovskite materials and solar cells with mixed cations and halide anions, ACS Appl. Mater. Interfaces 9 (2017) 30197–30246, https://doi.org/10.1021/acsami.7b06001.
[52] Private communication from E.J.J-P.
[53] A. García-Fernández, E.J. Juarez-Perez, S. Castro-García, M. Sánchez-Andújar, L. K. Ono, Y. Jiang, Y. Qi, Benchmarking chemical stability of arbitrarily mixed 3D hybrid halide perovskites for solar cell applications, Small Methods (2018), 1800242, https://doi.org/10.1002/smtd.201800242.
[54] Formamidinium based halide perovskites form carbon nitride residue like the FABr and FAI salts studied here. Private communication from E. J. Jet Propuls..